

Gap Opening in Twisted Double Bilayer Graphene by Crystal fields

Peter Rickhaus,^{*,†} Giulia Zheng,[†] Jose L. Lado,[‡] Yongjin Lee,[†] Annika
Kurzmann,[†] Marius Eich,[†] Riccardo Pisoni,[†] Chuyao Tong,[†] Rebekka Garreis,[†]
Carolin Gold,[†] Michele Masseroni,[†] Takashi Taniguchi,[§] Kenji Wantanabe,[§]
Thomas Ihn,[†] and Klaus Ensslin[†]

[†]*Solid State Physics Laboratory, ETH Zürich, CH-8093 Zürich, Switzerland*

[‡]*Department of Applied Physics, Aalto University, Espoo, Finland*

[¶]*Institute for Theoretical Physics, ETH Zurich, 8093 Zurich, Switzerland*

[§]*National Institute for Material Science, 1-1 Namiki, Tsukuba 305-0044, Japan*

E-mail: peterri@phys.ethz.ch

Supporting Information

Zero density lines

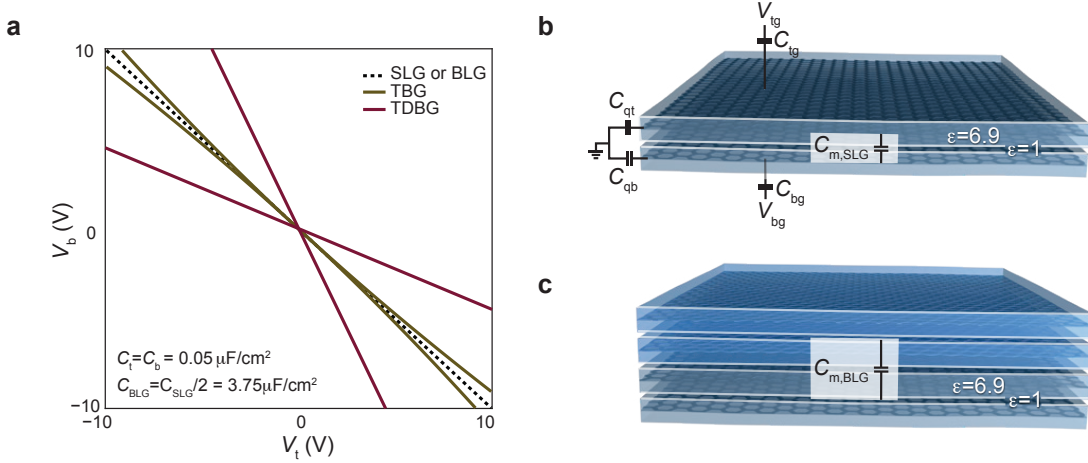


Figure S1: a) Zero-density lines for single-layer graphene (SLG, dashed line), bilayer graphene (BG, dashed line), large-angle twisted bilayer graphene (TBG, brown), large-angle twisted double bilayer graphene (TDBG, red) b) Electrostatic model for large-angle twisted bilayer graphene and c) large-angle twisted double bilayer graphene, where the geometric capacitance $C_{\text{m,BG}} = C_{\text{m,SLG}}/2$.

Following the argumentation of Ref.¹ and using that $C_b/C_m \ll 1$ and $C_t/C_m \ll 1$, the zero density lines in the gate-gate map have slopes:

$$\left. \frac{\partial V_t}{\partial V_b} \right|_{n_b=0} = -\frac{C_b}{C_t} \left(1 + \frac{C_t}{C_m} + \frac{C_{\text{qt}}}{C_m} \right) \approx -\frac{C_b}{C_t} \left(1 + \frac{C_{\text{qt}}}{C_m} \right) \quad (\text{S1})$$

$$\left. \frac{\partial V_b}{\partial V_t} \right|_{n_t=0} = -\frac{C_t}{C_b} \left(1 + \frac{C_b}{C_m} + \frac{C_{\text{qb}}}{C_m} \right) \approx -\frac{C_t}{C_b} \left(1 + \frac{C_{\text{qb}}}{C_m} \right) \quad (\text{S2})$$

$$\left. \frac{\partial V_b}{\partial V_t} \right|_{n_{\text{tot}}=0} = -\frac{C_t}{C_b} \cdot \frac{1 + C_b C_{\text{qb}} + C_m (C_{\text{qb}} + C_{\text{qt}})}{1 + C_t C_{\text{qt}} + C_m (C_{\text{qb}} + C_{\text{qt}})} \approx -\frac{C_t}{C_b} \quad (\text{S3})$$

In Fig. S1a we show the impact of these formulas for different structures in a symmetric geometry. For single- (SLG) and Bernal bilayer graphene (BG), the zero density line consists of a single line with slope $-C_t/C_b$. For BG, the applied perpendicular electric field along this line is changing, and it is zero at the origin. A splitting of the zero density line can be observed for large-angle twisted BG, with the amount of splitting given by $(1 + C_q/C_m)$. The behavior is non-linear, since $C_q \propto \sqrt{n}$. This is different for large angle TDBG where $C_q \propto \text{const.}$ (red lines in the figure). For the depicted lines in the figure we used a symmetric configuration with $C_t = C_b = 0.05 \mu\text{F}/\text{cm}^2$. As geometric capacitances between the twisted

layers we use $C_{m,BG} = C_{m,SLG}/2 = 3.75 \mu\text{F}/\text{cm}^2$ and for the quantum capacitances standard values from literature.

In Fig. S1b we schematically draw the electrostatic model for large-angle twisted bilayer graphene. The geometric capacitance between the layers, $C_{m,SLG}$, can be obtained by considering two "thick" graphene layers with relative dielectric constant $\epsilon_g = 6.9$ and thickness $d_g = 2.6 \text{ \AA}$ separated by vacuum ($\epsilon = 1$) and $d = 0.8 \text{ \AA}$. In this case:

$$C_{m,SLG} = \frac{\epsilon_g \epsilon_0}{d_g} + \frac{\epsilon_0}{d}$$

In the case of TDBG, between the center of charges of the top BG and the bottom BG there are two graphene layers and two times a gap with vacuum, therefore

$$C_{m,BG} = \frac{\epsilon_g \epsilon_0}{2d_g} + \frac{\epsilon_0}{2d} = \frac{C_{m,SLG}}{2}$$

Extracting the slopes from the measurements

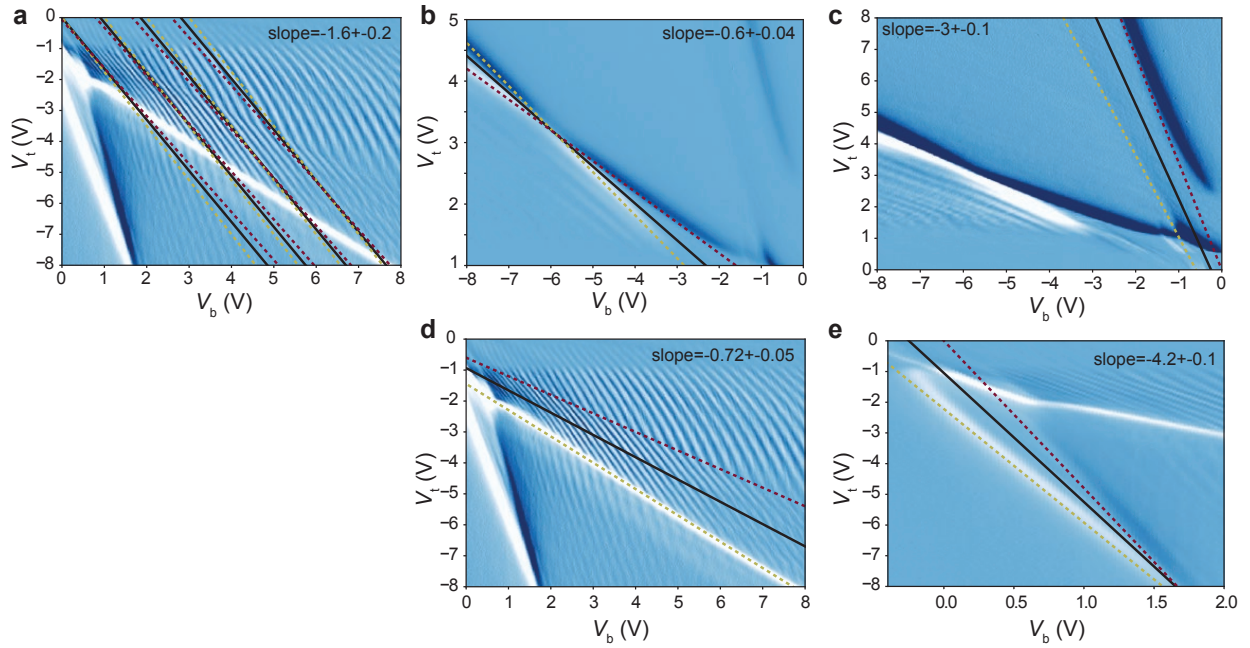


Figure S2: Extracting the slopes of the zero density lines

Here we describe our procedure to extract the slopes of the zero density condition from the measurement. In Fig.S2a we consider the slope of the Fabry-Pérot oscillations of the bottom layer if the top layer is gapped. We find

$$\left. \frac{\partial V_b}{\partial V_t} \right|_{n_{\text{tot}}=0} \approx -\frac{C_t}{C_b} \approx -1.6 \pm 0.2$$

which is in reasonable agreement with the expected slope from electrostatic considerations considering the measured thickness of top and bottom hBN i.e. $C_t/C_b = d_b/d_t = 1.5$. In Figs.S2b-e we determine the slopes of the zero density lines by fitting a line in the middle of the gap and we find:

$$\begin{aligned} \left. \frac{\partial V_b}{\partial V_t} \right|_{n_t=0, n_b < 0} &\approx -0.6 \pm 0.04, & \left. \frac{\partial V_b}{\partial V_t} \right|_{n_t=0, n_b > 0} &\approx -0.72 \pm 0.05 \\ \left. \frac{\partial V_b}{\partial V_t} \right|_{n_b=0, n_t < 0} &\approx -4.2 \pm 0.1, & \left. \frac{\partial V_b}{\partial V_t} \right|_{n_b=0, n_t > 0} &\approx -3 \pm 0.1 \end{aligned}$$

Electron-hole asymmetry

We notice that the slopes of the zero-density lines deviate depending on the charge carrier polarity of the other BG. We attribute this effect to a different effective mass for electrons (m_e^*) or holes (m_h^*) which changes the screening. With

$$\begin{aligned} C_{qte} = C_{qbe} = C_{qe} = e^2 \mathcal{D}_e = e^2 \frac{2m_e^*}{\hbar^2} &\quad \text{for electrons} \\ C_{qth} = C_{qbh} = C_{qh} = e^2 \mathcal{D}_h = e^2 \frac{2m_h^*}{\hbar^2} &\quad \text{for holes} \end{aligned}$$

we modify the above equations to

$$\left. \frac{\partial V_t}{\partial V_b} \right|_{n_b=0, n_t > 0} \approx -\frac{C_b}{C_t} \left(1 + \frac{C_{qe}}{C_m} \right) \quad \left. \frac{\partial V_t}{\partial V_b} \right|_{n_b=0, n_t < 0} \approx -\frac{C_b}{C_t} \left(1 + \frac{C_{qh}}{C_m} \right) \quad (\text{S4})$$

$$\left. \frac{\partial V_b}{\partial V_t} \right|_{n_t=0, n_b > 0} \approx -\frac{C_t}{C_b} \left(1 + \frac{C_{qe}}{C_m} \right) \quad \left. \frac{\partial V_b}{\partial V_t} \right|_{n_t=0, n_b < 0} \approx -\frac{C_t}{C_b} \left(1 + \frac{C_{qh}}{C_m} \right) \quad (\text{S5})$$

$$(\text{S6})$$

By using the experimentally extracted value for C_t/C_b , for the zero-density line of the top BG, we then determine the asymmetry

$$\frac{C_{qe}}{C_{qh}} = \frac{m_e^*}{m_h^*} = 0.73 \pm 0.19$$

and for the bottom zero density line

$$\frac{C_{qe}}{C_{qh}} = \frac{m_e^*}{m_h^*} = 0.54 \pm 0.09$$

In average:

$$\frac{m_e^*}{m_h^*} = 0.63 \pm 0.1 \quad (\text{S7})$$

Note that this is independent of the value of C_m .

In Fig.S3a we show the influence of different electron/hole masses on the zero density

lines. In the brown shaded area, the top BG is p-doped. The heavier mass in the valence band leads to a stronger screening of the top-gate. Therefore, a large voltage V_t needs to be applied in order to reach the zero-density line in the bottom layer (red solid line) compared to the case where the masses are equal (red dashed lines). I.e. if the top BG is p-doped, the slope of the red solid line is less steep than the red dashed line, and vice-versa if the top BG is n-doped.

In Fig.S3b we plot again the DFT calculation for low energies (see main text) and added dashed lines as guide to the eyes. Clearly, m_e^* and m_h^* differ.

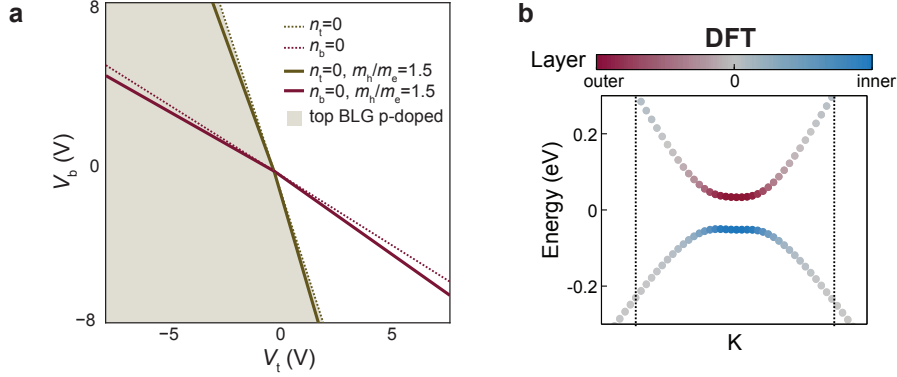


Figure S3: a) Zero density lines if an electron-hole asymmetry is assumed. b) Such asymmetry is obviously present in the DFT band structure. Dashed lines are guides to the eye.

Estimation of C_m

We can estimate the geometric capacitance by making assumptions for the quantum capacitance, i.e. $C_{qe} = e^2 \cdot 2m_e^*/\hbar^2\pi$ with $m_e^* = 0.80 \cdot 0.03m_e$ and $C_{qh} = e^2 \cdot 2m_h^*/\hbar^2\pi$ with $m_h^* = 1.26m_e^*$ such that $m_e^*/m_h^* = 0.63$. By inserting this assumption and the measured slopes into Eq.S6, we find

$$C_m = 3.5 \pm 1 \mu\text{F}/\text{cm}^2 \quad (\text{S8})$$

We can estimate whether this number is reasonable by comparing to the measured capacitance between two single-layer graphene sheets, which was $C_{m,\text{SLG}} = 7.5 \pm 0.7 \mu\text{F}/\text{cm}^2$.¹ Within the error bars, we measure half this capacitance, as expected.

Determining applied fields to the top/bottom BG

For just one bilayer system, the displacement field between the two single layers is roughly

$$D = \frac{1}{2\epsilon_0}(C_t V_t - C_b V_b)$$

Where C_t (C_b) is the capacitance between the top (bottom) graphene layer and the top (bottom) gate and V_t (V_b) the voltage applied to the top (bottom) gate.

For the TDBG system and for zero density in the top two layers (i.e. $n_t = 0$ and $V_{\text{tBG}} = 0$), we notice that the lower two layers act as a gate on the upper layers, i.e. we replace $C_b V_b$ by $C_m V_{\text{bBG}}$ (the product of measured interlayer capacitance between the BG sheets C_m and the electrochemical potential of the lower layer V_{bBG}) and use that the Fermi energy in the bottom layer is

$$E_{F,b} = eV_{\text{bBG}} = \frac{\hbar^2}{2m^*} \pi n_b = \frac{e^2}{C_{\text{qb}}} n_b$$

Therefore, the displacement field between the upper two layers is:

$$D_{\text{top}} = -\frac{1}{2\epsilon_0} (C_t V_t - \frac{C_m}{C_q} \cdot e n_b) \quad (\text{S9})$$

We note that we have used two approximations: First, the parabolic dispersion of the bottom BG, i.e. no trigonal warping. For large enough $E_{F,b}$, this approximation is valid. Second, we considered the gating effect of the bottom BG on the top BG and neglected that the bottom BG consists of two layers with different electrochemical potential. Also this approximation is valid for large enough $E_{F,b}$.

In analogy we find

$$D_{\text{bottom}} = \frac{1}{2\epsilon_0} (C_b V_b - \frac{C_m}{C_q} \cdot e n_t) \quad (\text{S10})$$

The relation between D and the gap has to be solved self-consistently, but for sufficiently large D it is roughly linear, with a slope of $195 \text{ meV}/(\text{Vnm}^{-1})$.

Measurements on device 2

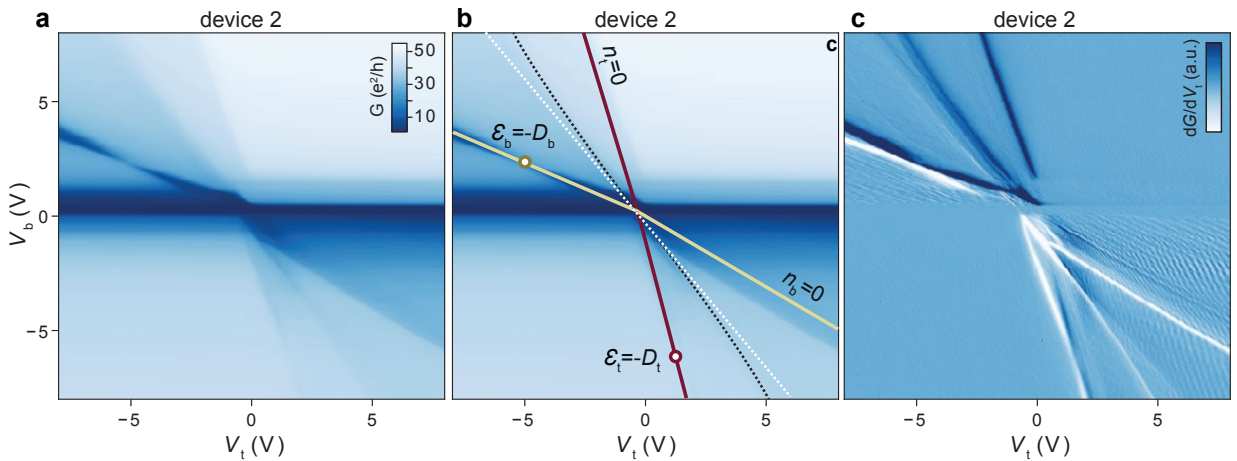


Figure S4: a) $G(V_t, V_b)$ for the second device. b) Similar to the main text, we indicate lines of zero density. c) Numerical derivative dG/dV_t of the data.

We fabricated a second TDBG device which exhibits comparable results. The main differences are:

- The different thickness of top- and bottom hBN ($d_t = 49$ nm, $d_b = 56$ nm, as compared to device 1 with $d_t = 60$ nm, $d_b = 90$ nm) results in larger capacitances and thus a stronger gating effect and different slopes in the $G(V_t, V_b)$ maps.
- The groundstate resistance is higher, i.e. the highest measured resistance in device 2 is $R_{\max} = 94$ k Ω compared to $R_{\max} = 10$ k Ω in device 1. This may originate from higher quality of the stack.
- Unfortunately, the top gate covers an area, where a single-layer flake is twisted on top of a bilayer flake. We call this area twisted single-layer bilayer graphene TSLBG area. The TSLBG area does not connect source and drain contacts, therefore the observation of high resistance is possible. However, the TSLBG area leads to the appearance of a curved zero density line in the conductance map (white dashed line in FigS4b, originating from the single-layer graphene flake (compare to Fig.S1a) and a straight line (black dashed line in FigS4b) that is caused by the bilayer graphene in this area. The presence of the TSLBG area does not affect the analysis of the TDBG features.

We apply the above discussed capacitance model, considering the modified values for C_t and C_b , and obtain the crystal fields present in this device. We find similar values as for device 1, i.e.

$$\begin{aligned}\mathcal{E}_t &= 0.11 \text{ V/nm} \\ \mathcal{E}_b &= -0.12 \text{ V/nm}\end{aligned}$$

With a slope of with a slope of $195 \text{ meV}/(\text{Vnm}^{-1})$ we find gaps of:

$$\begin{aligned}\Delta_t &= 21 \text{ meV} \\ \Delta_b &= 23 \text{ meV}.\end{aligned}$$

Measurements on device 3 with a global topgate

In figure S8 we show the gate-gate map $G(V_t, V_b)$ of a device which has a global topgate, which we realized by evaporating an additional layer of AlO_x after contacting the device and before depositing the top gate. As opposed to devices 1 and 2, the gap appears only in the central region of the plot (around $V_t, V_b = 0, 0$), i.e. there is no high resistive state present around $V_b = 0$ for arbitrary V_t , as expected for a global topgate. The zero density lines appear to be more 'blurry' in device 3 compared to devices 2 and 1. We attribute this to the fact that the region that we probe with this device is significantly larger ($2 \times 3 \mu\text{m}^2$) than the region that we probe with the local topgate ($0.4 \times 3 \mu\text{m}^2$), making the conductance more affected by local charge density variations due to disorder. Nevertheless, we do observe charge density lines which are in good agreement with our capacitance model. I.e. the red and yellow line in figure S8b are obtained by inserting the geometric capacitances of this

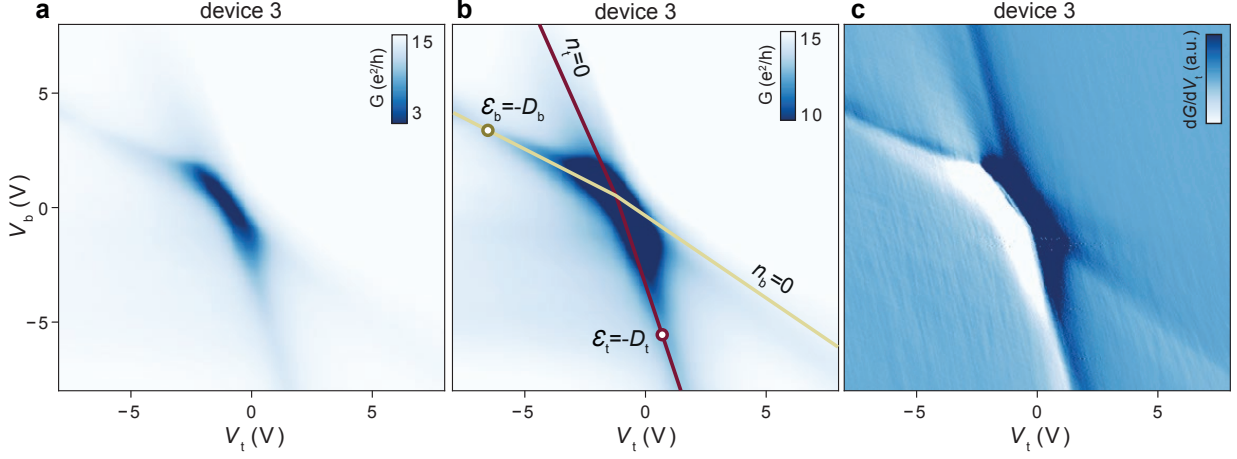


Figure S5: a) $G(V_t, V_b)$ for the third device with a global topgate. b) Device 3 with calculated zero density lines $n_t = 0$ and $n_b = 0$. c) Numerical derivative dG/dV_t of the data.

specific device into equation S6. We use $\epsilon_r = 9.5$ for the AlO_x layer. At the marked positions of gap closing in the top/bottom layer we find:

$$\begin{aligned}\mathcal{E}_t &= 0.13 \text{ V/nm} \\ \mathcal{E}_b &= -0.14 \text{ V/nm}\end{aligned}$$

With a slope of with a slope of $195 \text{ meV}/(\text{Vnm}^{-1})$ we find gaps of:

$$\begin{aligned}\Delta_t &= 25 \text{ meV} \\ \Delta_b &= 27 \text{ meV}.\end{aligned}$$

A model for the Fabry-Pérot resonances

To obtain the Fabry-Pérot oscillation periodicity, we calculate the densities using :

$$\begin{aligned}n_t &= a_t V_b + b_t V_t \\ n_b &= a_b V_b + b_b V_t\end{aligned}$$

where

$$\begin{aligned}a_t &= \frac{C_b C_m C_q}{(C_q(C_q + C_{tg}) + C_b(C_m + C_q + C_t) + C_m(2C_q + C_t))e} \\ b_t &= \frac{C_q C_t (C_b + C_m + C_q)}{(C_q(C_q + C_t) + C_b(C_m + C_q + C_t) + C_m(2C_q + C_t))e} \\ a_b &= \frac{C_q C_b (C_m + C_q + C_t)}{(C_q(C_q + C_t) + C_b(C_m + C_q + C_t) + C_m(2C_q + C_t))e} \\ b_b &= \frac{C_q C_m C_t}{(C_q(C_q + C_t) + C_b(C_m + C_q + C_t) + C_m(2C_q + C_t))e}.\end{aligned}$$

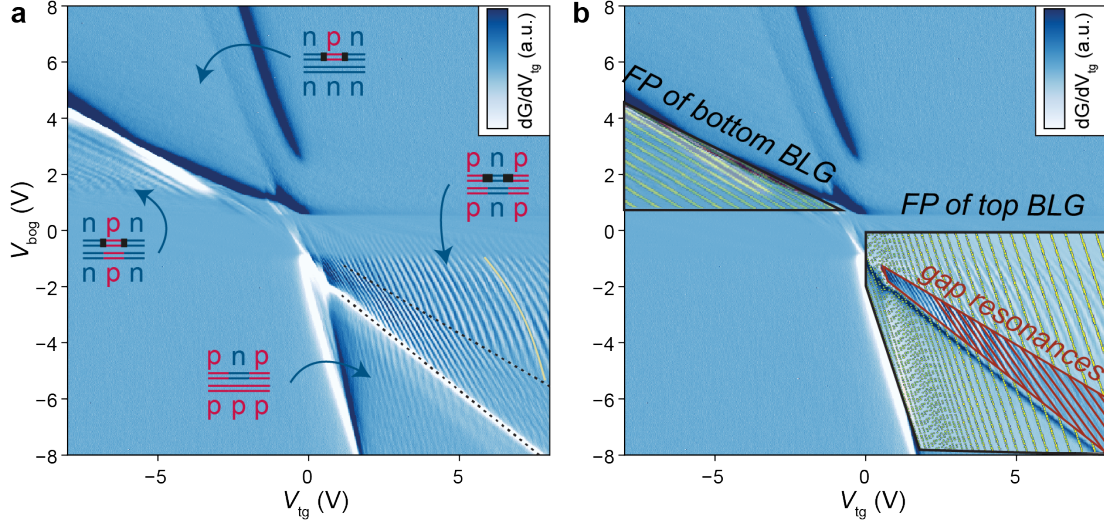


Figure S6: **a** Numerical derivative of the measured conductance as a function of the gate voltages. Insets show the charge configurations of the device (p = holes, n = electrons). The black dashed lines delimit a region that corresponds to the opening of a gap in the bottom BLG (see main text). The bending of the yellow line is due to a non-constant cavity size (see main text). **b** Plots of FP resonances calculated with a capacitance model on top of the experimental measurement. The black lines outline the calculations made with the capacitance model of tBBG while the red lines are calculated with the capacitance model of BLG. Lines with very small spacing are not plotted.

From the resulting density maps we calculate the Fabry-Pérot interference pattern using:

$$\frac{\lambda}{2}N = L,$$

where $L = 400$ nm is the width of the top gate and N is a natural number. Therefore, knowing that $\lambda = 2\pi/k$, with $k = \sqrt{\pi n_i}$ ($i = t, b$), we obtain the condition

$$n_i = \frac{\pi N^2}{L^2}. \quad (\text{S11})$$

Plotting this condition in a gate-gate map yields the FP pattern in the top and bottom bilayer that are depicted on top of the experimental measurement in figure S6.

Figure S6 represents the numerical derivative of the measured conductance with respect to the top gate $\partial G/\partial V_{tg}$, which allows us to observe the FP resonance pattern. On the upper left corner of the map we recognize FP interferences that belong to the pn-junction in the bottom BLG. They match reasonably well with the resonances calculated for the bottom layer in the previous section, which are plotted on top of the corresponding region in figure S6 b. The same is valid for the top bilayer resonances in the bottom right corner, except for a change in slope (yellow line in figure S6 a) due to an increase of the cavity size at low densities (see e.g. Supporting Information of Ref. ²), which is not captured in our model.

A third slope of the interference pattern is observed between the black lines of figure S6 a.

This pattern matches reasonably well with the plot of FP resonances in dual gated BLG that we show in red in figure S6 b. These plots were obtained by applying the FP condition (eq S11) using the calculated density of only one BLG. From these results we deduce that the top BLG in this area is not affected by the screening of the bottom BLG, which is possible if the Fermi energy in the bottom BLG is in a gap. This demonstrates that the region of reduced conductance around the zero density lines observed indeed correspond to gapped regions.

The mid-gap states in this region may be responsible for the slight difference between the predicted and the measured interference pattern in the gap: in our calculations we approximate the bottom BLG as a charge neutral layer, while instead it may contain non-conducting mid-gap states which can give a small contribution to the screening.

Thermal activation behavior of device 1

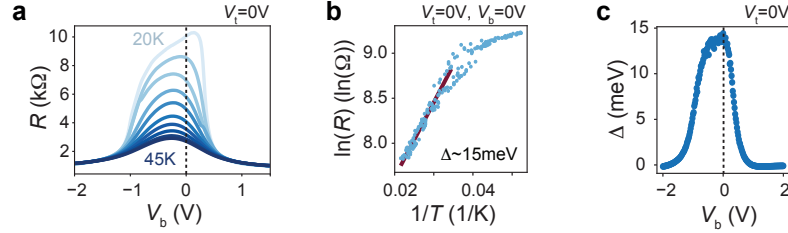


Figure S7: a) $R(V_b)$ for $V_t = 0$ and temperatures between 20 K and 45 K reveal the thermal activation of the gap in the ground state of device 1. b) In an Arrhenius plot ($V_t = V_b = 0$), the slope at high temperatures (red line) corresponds to a gap of $\Delta = 15$ meV. In c) we plot the extracted $\Delta(V_b)$.

In figure S7 we show the thermally activated behavior of device 1 (local topgate). We extract the gap as a function of V_b by setting $V_t = 0$.

Measurements on device 3 with a global topgate

In figure S8 we show the gate-gate map $G(V_t, V_b)$ of a device which has a global topgate, which we realized by evaporating an additional layer of AlO_x after contacting the device and before depositing the top gate. As opposed to devices 1 and 2, the gap appears only in the central region of the plot (around $V_t, V_b = 0, 0$), i.e. there is no high resistive state present around $V_b = 0$ for arbitrary V_t , as expected for a global topgate. The zero density lines appear to be more 'blurry' in device 3 compared to devices 2 and 1. We attribute this to the fact that the region that we probe with this device is significantly larger ($2 \times 3 \mu\text{m}^2$) than the region that we probe with the local topgate ($0.4 \times 3 \mu\text{m}^2$), making the conductance more affected by local charge density variations due to disorder. Nevertheless, we do observe charge density lines which are in good agreement with our capacitance model. I.e. the red and yellow line in figure S8b are obtained by inserting the geometric capacitances of this

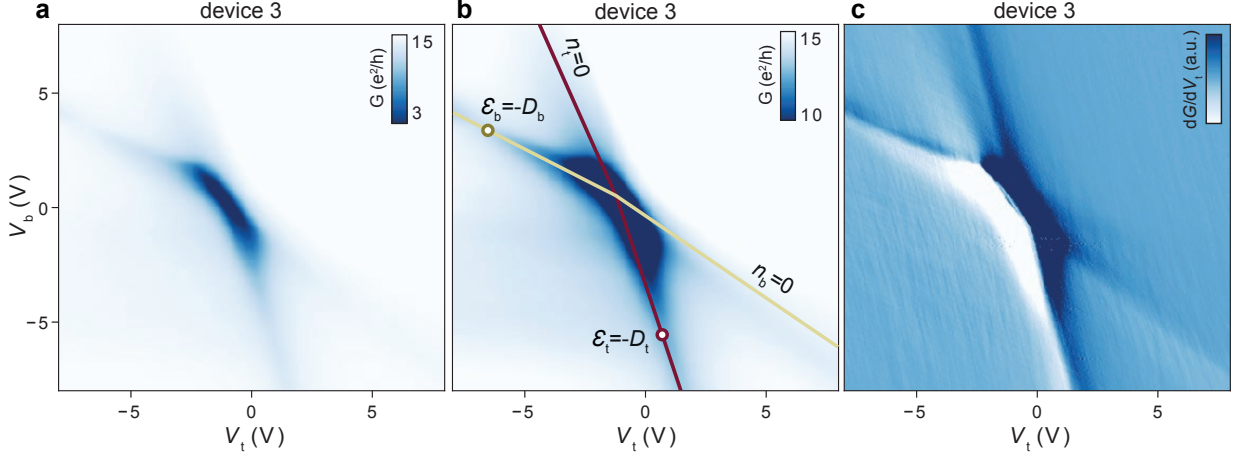


Figure S8: a) $G(V_t, V_b)$ for the third device with a global topgate. b) Device 3 with calculated zero density lines $n_t = 0$ and $n_b = 0$. c) Numerical derivative dG/dV_t of the data.

specific device into equation S6. We use $\epsilon_r = 9.5$ for the AlO_x layer. At the marked positions of gap closing in the top/bottom layer we find:

$$\begin{aligned}\mathcal{E}_t &= 0.13 \text{ V/nm} \\ \mathcal{E}_b &= -0.14 \text{ V/nm}\end{aligned}$$

With a slope of with a slope of $195 \text{ meV}/(\text{Vnm}^{-1})$ we find gaps of:

$$\begin{aligned}\Delta_t &= 25 \text{ meV} \\ \Delta_b &= 27 \text{ meV}.\end{aligned}$$

Gate maps at different temperatures

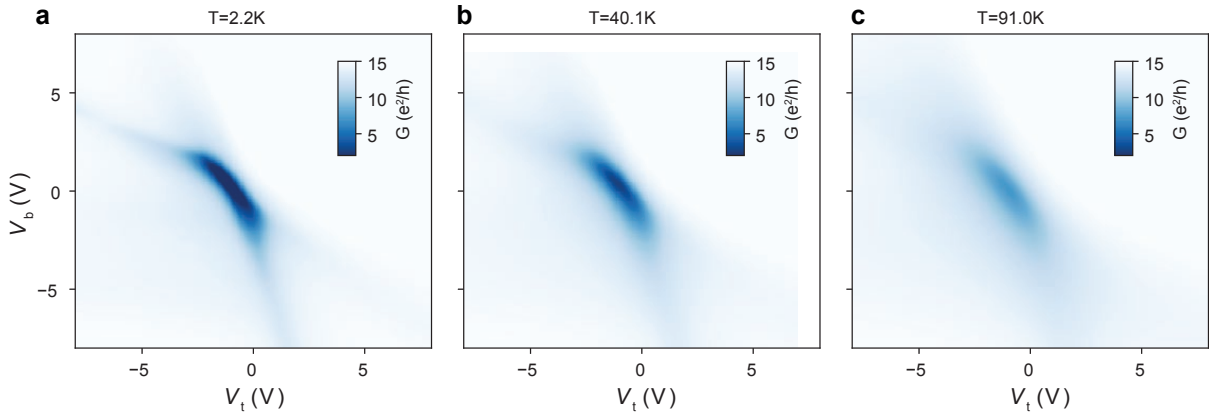


Figure S9: $G(V_t, V_b)$ of device 3 at different temperatures.

In figure S9 we show the gate-gate map $G(V_t, V_b)$ of device 3 at different temperatures,

ranging from 2.2 K to 91 K.

Density functional theory methods

Computational details

Density functional theory calculations were performed for a structure of twisted double bilayer graphene with a relative rotation angle between the two Bernal stacked bilayers of 13 degrees. The unit cell consists on 152 carbon atoms, and the structure was fully relaxed including van der Waals forces using the Grimme scheme.^{3,4} The first principles calculations were performed with the plane-wave pseudopotential formalism as implemented in Quantum Espresso,^{5,6} using ultrasoft pseudopotentials^{7,8} and PBEsol exchange correlation functional.⁹

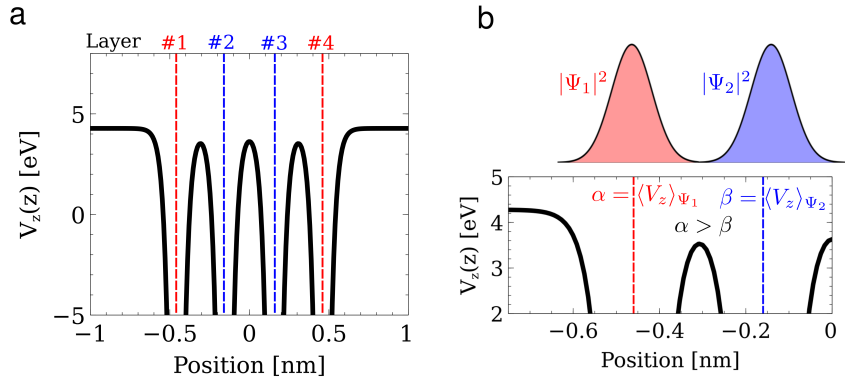


Figure S10: a) Average electrostatic potential in the z -direction as obtained from density functional theory. The dashed lines show the location of each graphene layer, and the Fermi energy corresponds to $V_z = 0$. Panel b) shows a sketch of the origin of the crystal field effect, highlighting that Wannier orbitals in the outer layers will feel a higher electrostatic potential, effectively increase the onsite energy in the outer layers and creating a small negative charge in the inner layers.

Microscopic origin of the crystal field effect

We now address the microscopic origin of the crystal field contribution in the TDBG using as starting point the first principles results, which can be easily rationalized combining the selfconsistent Kohn-Sham potential with first order perturbation theory.

We start with $V(x, y, z)$ the electronic potential as obtained from solving the Kohn-Sham equations with density functional theory, which gives access to the effective potential in each point of the space in the twisted bilayer unit cell. We define the average potential in the xy -plane, parallel to the graphene planes as

$$V_z(z) = \frac{1}{A} \int_{UC} V(x, y, z) dx dy \quad (\text{S12})$$

where \int_{UC} denotes integral of the TDBG unit cell and A is the area of the unit cell in the xy plane. The previous average potential as obtained from the first principles method is shown in Fig. S10a. We now take a $\Psi_i(z)$ the Wannier wavefunction of an electron localized in layer i , where we have integrated out the xy dependence, and we assume to have analogous z -profiles for the four different layers. The onsite energies α, β in layer 1 and 2 can be computed as

$$\begin{aligned}\alpha &= \int V_z(z) |\Psi_1(z)|^2 dz \\ \beta &= \int V_z(z) |\Psi_2(z)|^2 dz\end{aligned}\quad (\text{S13})$$

with the onsite difference between the layers $\delta = \alpha - \beta$. It can be easily seen by inspection of the potential profile V_z of Fig. S10a that the integrals α and β will give different results. In particular, since the layer 1 is closer to the outer region with higher potential, the onsite energy of the outer layers will be higher than the one of the inner layers (Fig. S10b). This yields that for electrons it is energetically favorable to sit in the two inner layers, creating a small internal electric field that yields the inner layers negatively charged and the outer ones positively charged.

Influence of the hBN substrate

Estimate from monolayer graphene encapsulated in hBN

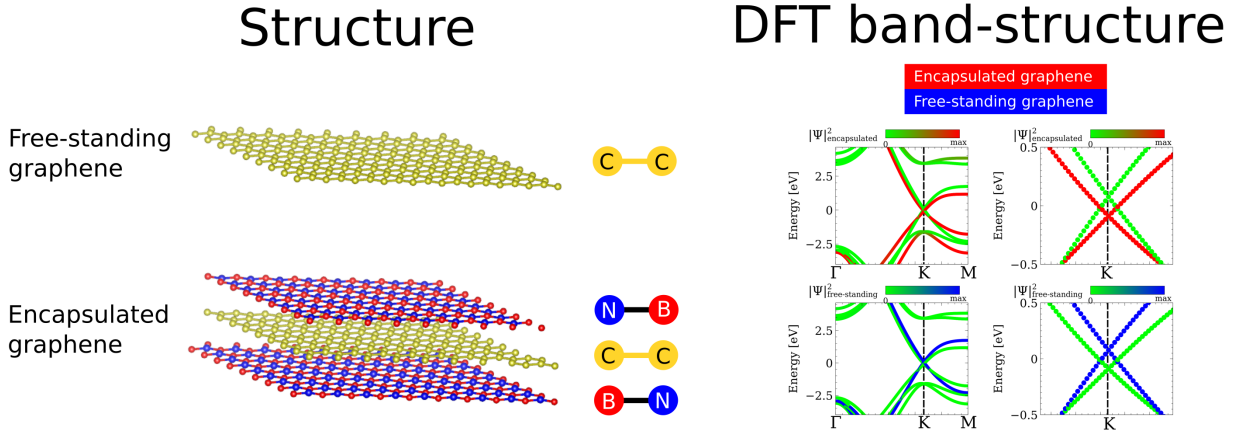


Figure S11: a) Representation of the crystal structure to qualitatively estimate the effect of hBN on the crystal fields. The free-standing graphene is separated by vacuum from the encapsulated graphene and the two systems are decoupled. b) Band structures of the structure represented in figure a), calculated with DFT.

In the first principle calculations, the top and bottom hBN is neglected in order to reduce the computational cost of the problem. But, because the presence of the hBN lattices influence the crystal field effect, it is relevant to understand their impact. For this reason we compute a structure that allows to estimate their effect on a single layer of graphene, and compare it with the energy dispersion of free standing graphene. Such a structure is schematically represented in figure S11, where the two SLGs are spatially separated by a

large distance. In this way we compute a unit cell with two decoupled graphene layers, an encapsulated and a free-standing one, such that we obtain the energy difference of the two situations (figure S11). The result shows a splitting of ~ 120 meV between the Dirac points of the two SLGs, where the encapsulated graphene has a lower energy. From this observation we deduce that one hBN layer can shift the potential of a graphene layer in its vicinity by ~ 60 meV. Therefore, each hBN layer reduces the electrostatic potential of a neighboring graphene layer by 60 meV

By simply subtracting the previous 60 meV from the gap computed with free-standing tBBG, we estimate $\Delta_0 \approx 20$ meV for encapsulated tBBG, which is of the same order as the experimentally measured gap. Notice that, in order to have a small enough unit cell, we had to stretch the bonds of the hBN lattice.

Full calculation of twisted double bilayer graphene encapsulated in hBN

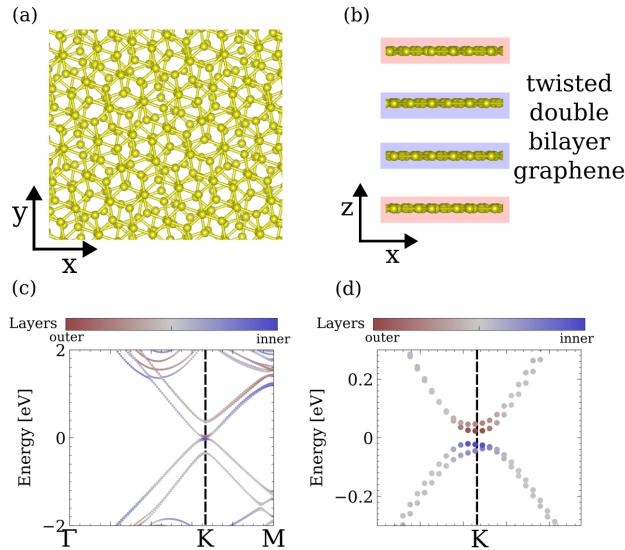


Figure S12: a,b) Sketch of the twisted double bilayer structure without the hBN encapsulation and a rotation angle of 21.8° . Panels c,d) show the first principles band structure, showing that the top of the valence band is localized in the two inner layers, which is associated with the crystal field induced gap.

We now address from first principles a twisted double bilayer together with the hBN encapsulation. Since the calculations involving hBN are computationally expensive, here we will focus on an encapsulated double bilayer structure with a rotation angle of 21.8° , i.e. a large angle double bilayer which shows an analogous crystal field induced gap to the experimental situation. For the sake of completeness, we will compare the electronic structure of such twisted double bilayer with and without the hBN encapsulation, showing that no qualitative change is introduced by the hBN substrate. We first focus on the twisted double bilayer without hBN encapsulation and a rotation angle of 21.8° (Fig. S12a,b). As shown in the first principles band structures of Fig. S12c,d, an analogous crystal field induced gap appears in the system, creating a small charge imbalance between the inner and outer layers.

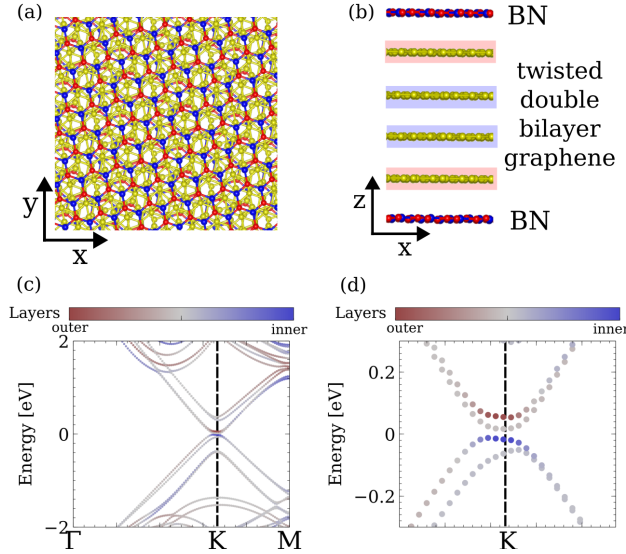


Figure S13: a,b) Sketch of the twisted double bilayer structure with the hBN encapsulation and a rotation angle of 21.8° . The first principles band structure c,d) shows an analogous behavior to the case without hBN, but presenting a smaller crystal-field induced gap.

This is the same phenomenology as it was observed in the twisted structure at 13 degrees rotation, which highlights that the crystal field induced gap happens for generic large angles. We now move on to the twisted double bilayer with hBN encapsulation and a rotation angle of 21.8° (Fig. S13a,b). In this situation, we also observe a crystal field induced gap in the encapsulated twisted double bilayer (Fig. S13c,d), similar to the one found without the encapsulation. The top of the valence band is also localized in the inner layers, showing that this encapsulated system will also present a small charge imbalance. The effect of the hBN is to slightly decrease the value of the crystal field induced gap, yet without creating a qualitative change in the electronic structure.

References

- (1) Peter Rickhaus, Ming-hao Liu, Marcin Kurpas, Annika Kurzmann, Yongjin Lee, Hiske Overweg, Riccardo Pisoni, Takashi Tamaguchi, Kenji Watanabe, Klaus Richter, Klaus Ensslin, and Thomas Ihn, “The Electronic Thickness of Graphene,” arXiv:1907.00582v1, 1–15 (2019), arXiv:1907.00582v1 .
- (2) Clevin Handschin, Péter Makk, Peter Rickhaus, Romain Maurand, Kenji Watanabe, Takashi Taniguchi, Klaus Richter, Ming-Hao Liu, and Christian Schönenberger, “Giant Valley-Isospin Conductance Oscillations in Ballistic Graphene,” *Nano Lett.* **17**, 5389–5393 (2017).
- (3) Stefan Grimme, “Semiempirical GGA-type density functional constructed with a long-range dispersion correction,” *Journal of Computational Chemistry* **27**, 1787–1799 (2006).

- (4) Vincenzo Barone, Maurizio Casarin, Daniel Forrer, Michele Pavone, Mauro Sambi, and Andrea Vittadini, “Role and effective treatment of dispersive forces in materials: Polyethylene and graphite crystals as test cases,” *Journal of Computational Chemistry* **30**, 934–939 (2009).
- (5) Paolo Giannozzi, Stefano Baroni, Nicola Bonini, Matteo Calandra, Roberto Car, Carlo Cavazzoni, Davide Ceresoli, Guido L Chiarotti, Matteo Cococcioni, Ismaila Dabo, Andrea Dal Corso, Stefano de Gironcoli, Stefano Fabris, Guido Fratesi, Ralph Gebauer, Uwe Gerstmann, Christos Gougoussis, Anton Kokalj, Michele Lazzeri, Layla Martin-Samos, Nicola Marzari, Francesco Mauri, Riccardo Mazzarello, Stefano Paolini, Alfredo Pasquarello, Lorenzo Paulatto, Carlo Sbraccia, Sandro Scandolo, Gabriele Sclausero, Ari P Seitsonen, Alexander Smogunov, Paolo Umari, and Renata M Wentzcovitch, “QUANTUM ESPRESSO: a modular and open-source software project for quantum simulations of materials,” *Journal of Physics: Condensed Matter* **21**, 395502 (2009).
- (6) P Giannozzi, O Andreussi, T Brumme, O Bunau, M Buongiorno Nardelli, M Calandra, R Car, C Cavazzoni, D Ceresoli, M Cococcioni, N Colonna, I Carnimeo, A Dal Corso, S de Gironcoli, P Delugas, R A DiStasio, A Ferretti, A Floris, G Fratesi, G Fugallo, R Gebauer, U Gerstmann, F Giustino, T Gorni, J Jia, M Kawamura, H-Y Ko, A Kokalj, E Küçükbenli, M Lazzeri, M Marsili, N Marzari, F Mauri, N L Nguyen, H-V Nguyen, A Otero de-la Roza, L Paulatto, S Poncé, D Rocca, R Sabatini, B Santra, M Schlipf, A P Seitsonen, A Smogunov, I Timrov, T Thonhauser, P Umari, N Vast, X Wu, and S Baroni, “Advanced capabilities for materials modelling with quantum ESPRESSO,” *Journal of Physics: Condensed Matter* **29**, 465901 (2017).
- (7) David Vanderbilt, “Soft self-consistent pseudopotentials in a generalized eigenvalue formalism,” *Phys. Rev. B* **41**, 7892–7895 (1990).
- (8) Andrea Dal Corso, “Pseudopotentials periodic table: From h to pu,” *Computational Materials Science* **95**, 337–350 (2014).
- (9) John P. Perdew, Adrienn Ruzsinszky, Gábor I. Csonka, Oleg A. Vydrov, Gustavo E. Scuseria, Lucian A. Constantin, Xiaolan Zhou, and Kieron Burke, “Restoring the density-gradient expansion for exchange in solids and surfaces,” *Phys. Rev. Lett.* **100**, 136406 (2008).